

Phase Transformation in Lithium Niobate-Lithium Tantalate Solid Solutions ($\text{LiNb}_{1-x}\text{Ta}_x\text{O}_3$)

Fatima El Azzouzi*, Detlef Klimm, Alexander Kapp, Leonard M. Verhoff, Nils A. Schäfer, Steffen Ganschow, Klaus-Dieter Becker, Simone Sanna, and Holger Fritze

F. El Azzouzi and H. Fritze, Institut für Energieforschung und Physikalische Technologien, Technische Universität Clausthal, Am Stollen 19B, 38640 Goslar, Germany, Email Address: fatima.ezzahrae.el.azzouzi@tu-clausthal.de

D. Klimm and S.Ganschow, Leibniz-Institut für Kristallzüchtung, Max-Born-Str. 2, 12489 Berlin, Germany

A. Kapp, L. M. Verhoff, N. Schäfer and S. Sanna, Institut für Theoretische Physik, Justus-Liebig-Universität Gießen, Heinrich-Buff-Ring 16, 35392 Gießen, Germany

K-D. Becker, Institut für Physikalische und Theoretische Chemie, Technische Universität Braunschweig, 38023 Braunschweig, Germany

Keywords: *lithium niobate-tantalate, phase transformation, mixed ferroelectrics, electric conductivity, high-temperature*

The investigation of the structural phase transition in the vicinity of the Curie temperature T_c of $\text{LiNb}_{1-x}\text{Ta}_x\text{O}_3$ crystals is motivated by the expected combination of advantageous high-temperature properties of LiNbO_3 and LiTaO_3 , including high piezoelectric modules and remarkable high-temperature stability, respectively. T_c marks the ultimate limit for exploiting the piezoelectric properties, however transition related structural modifications might impact this and other properties even below T_c .

Remarkably, the phase transition from the ferroelectric to the paraelectric phase, whose temperature strongly depends on the composition x , shows a significant drop in the activation energy of the electrical conductivity. The magnitude, temperature dependence and underlying mechanisms of this drop are discussed from a microscopic perspective. Molecular dynamics calculations in the framework of the density functional theory show that substantial displacements of the cations occur below T_c for both the end compounds LiNbO_3 and LiTaO_3 , and might thus affect the electrical conductivity. Above T_c , the migration of lithium ions is presumably facilitated by a shortened diffusion path for the most favorable jump of the lithium ions. Electronic contributions to the conductivity, which become important above 900 K, are explained within the polaronic picture by the formation and migration of free small polarons.

1 Introduction

The single crystals of lithium niobate (LiNbO_3 , LN) are well established in the field of optics. They are, for example, highly birefringent and exhibit high electro-optic coefficients. Moreover, the photoelastic as well as nonlinear optical properties are also distinctive [40, 9]. These unique characteristics make LN an indispensable material for various applications, such as electro-optic modulation, frequency conversion, and optical parametric oscillation [41]. Similarly, lithium tantalate (LiTaO_3 , LT) has also gained significant attention in various fields due to its large Non-Linear Optical (NLO) coefficients [27, 9] and resistance to photorefractive damage [39]. Further, the piezoelectric properties of LN and LT render them ideal candidates for acoustic wave devices [46, 18], holographic storage devices [12], channel waveguides [20, 16], periodically poled structures [43], and electro-optic deflectors [10].

Crystals of $\text{LiNb}_{1-x}\text{Ta}_x\text{O}_3$ (LNT) solid solutions comprises the two border components LN and LT, which share the same crystal structure (space group $R3c$) but differ in their lattice and positional parameters, as well as their melting and Curie temperatures [33, 44]. The Czochralski method is commonly used for growing LN and LT crystals, which have a congruent composition containing approximately 48.4 and 48.5 mol% Li_2O [5, 25, 19, 15], respectively. LN has a higher Curie temperature than LT. Also, LN exhibits higher piezoelectric coefficients but its high-temperature stability is poor due to its decomposition between 573 K and 1073 K [13]. On the other hand, LT crystals are shown to have better high-temperature stability which, for example, is connected with a lower electrical conductivity of LT above about 873 K [21]. However, the piezoelectric coefficients of LT crystals are lower than those of LN crystals [26, 34, 6]. To combine the superior properties of LN and LT, respectively, LNT crystals have been developed, with the aim of achieving both high piezoelectric coefficients and good high-temperature stability. This makes LNT crystals highly desirable for high-temperature applications and should allow for the fabrication of new devices including sensors for harsh environments.

The paraelectric to ferroelectric phase transitions of LN and LT are considered to be second-order phase transitions [37, 32]. In the case of LN, it occurs at fairly high temperature. Experimental data and theoretical modeling report transition temperatures for the congruent material in the range from 1413 K to 1475 K. A spontaneous polarization of $71 \mu\text{C}/\text{cm}^2$ is found at room temperature [41]. The structurally similar LT, however, has a lower phase transition temperature reported in the range from 874 K to 958 K [8, 28] and a spontaneous polarization of $60 \mu\text{C}/\text{cm}^2$ [8]. The structural transition T_c represents the upper limit at which devices exploiting the piezoelectric properties of the materials can be operated. However, as the phase transformation is known to be a continuous process [35, 31], transition related structural modifications might impact the materials properties even below T_c .

This study aims to uncover and explain changes in electrical conductivity that accompany the phase transition across various compositions. Our investigation involves experimental methods such as measuring electrical conductivity even above T_c , calorimetry, and theoretical exploration through *ab initio* molecular dynamics calculations executed on large supercells.

2 Methodology

2.1 Crystal growth

The LNT single crystals investigated here are grown at the Leibniz Institute for Crystal Growth in Berlin, Germany (IKZ), using the Czochralski method with induction heating. The starting materials are congruently melting LN and LT powders prepared from lithium carbonate (Li_2CO_3 , Alfa Aesar, 5 N), niobium pentoxide (Nb_2O_5 , H.C. Stark, 4N5), and tantalum pentoxide (Ta_2O_5 , Fox Chemicals, 4 N), all dried before use. Two different LNT crystals are prepared by mixing LN and LT powders with LT mass fractions of 18% and 34%. Crystal compositions of $x \approx 0.42$ and 0.64 result respectively. They are determined by averaging the distribution of Nb and Ta in the grown single crystals measured by Energy Dispersive Micro-X-ray Fluorescence (μ -XRF) analysis in a pre-vacuum environment (20 mbar) using a Bruker M4 TORNADO spectrometer. Within the crystal sections used for the experiments discussed below, a variation in the composition of $\delta x = 0.02$ is found. In the following, the term *composition* refers exclusively to x according to $\text{LiNb}_{1-x}\text{Ta}_x\text{O}_3$.

Seeds are pulled at a rate of 0.2 mm/h. The crystals grow along the [0001] direction (c-axis) in accordance with the orientation of the crystal seed. The process is carried out in a protective argon atmosphere with a small addition of oxygen (0.08 vol%). Details can be found in [1].

To enable comparison of LNT with LN and LT, congruent X-cut and Z-cut LN and LT wafers are purchased from Precision Micro-Optics Inc. (PMO, USA).

2.2 Sample preparation

The crystals are cut into rectangular plates of $5 \times 6 \text{ mm}^2$. The only exception represent the samples with $x = 0.64$. They are slightly smaller and show an irregular shape. To examine the electrical properties, platinum electrodes with a thickness of about $3 \mu\text{m}$ are deposited by screen printing on both surfaces of the samples using platinum paste (Ferro Corporation, No. 6412 0410). Subsequently, the samples are annealed at 1273 K for about an hour, with a heating rate of 2 K/min. Key information including sample name, composition, orientation, thickness and electrode size are given in Tab. 1.

2.3 Calorimetry

Differential scanning calorimetry (DSC) is performed using a thermal analyzer (NETZSCH STA 449C F3, Germany). According to ASTM E1269, three consecutive measurements are carried out under identical conditions with empty reference and sample crucibles (baseline), Al_2O_3 powder is used as standard with known $C_p(T)$ function. Four subsequent heating runs are conducted up to 1463 K in a flow mixture of 40 ml/min Ar and 20 ml/min O_2 , with isothermal segments for equilibration. The average $C_p(T)$ functions from the last three heating segments is used for further evaluation.

Table 1: Overview of the samples used in this study. The composition x refers to $\text{LiNb}_{1-x}\text{Ta}_x\text{O}_3$. The orientation denotes the crystallographic direction perpendicular to the largest surface.

Sample name	Composition x	Manufacturer	Orientation	Thickness [mm]	Electrode size [mm ²]
LN-X	0	PMO	X	0.5	5×6
LN-Z	0	PMO	Z	0.5	5×6
LNT42-Y	0.42	IKZ	Y	0.68	5×6
LNT42-Z	0.42	IKZ	Z	0.44	5×6
LNT64-Y	0.64	IKZ	Y	0.73	$\pi \times 3^2$
LNT64-Z	0.64	IKZ	Z	0.76	$\pi \times 2.5^2$
LT-X	1	PMO	X	0.5	5×6
LT-Z	1	PMO	Z	0.5	5×6

2.4 Molecular dynamics

Ab initio molecular dynamics as implemented in the Vienna Ab Initio Simulation Package (VASP) [24, 22, 23] is performed to model LiNbO_3 and LiTaO_3 within density functional theory at finite temperatures. An canonical NVT ensemble, controlled by the Nosé-Hover thermostat [29, 11] was simulated at different temperatures to gather information about the temperature dependent lattice dynamics. A Verlet algorithm with 2 fs time steps was used to integrate the equations of motion. A total simulation time of about 5 ps was considered. Due to the random initialization of the velocities, an equilibration time of about 0.5-1 ps is necessary, which is not considered in the evaluation of the AIMD trajectories. For the simulation of LN and LT, large supercells consisting of 128 Li cations, 128 Nb or Ta cations and 384 O anions were used. Thereby, the thermal expansion as calculated within the quasi-harmonic approximation is considered [2]. Due to the the supercell size in real space, the MD runs were performed on a single k -point, placed at the center of the Brillouin zone. Projector augmented waves, calculated according to Blöchl [4, 14] and implementing the PBEsol [30] formulation of the exchange-correlation potential are employed. The wave functions are expanded in a plane wave basis up to 400 eV.

From the AIMD runs, a real-time development of the polarization can be extrapolated. We employ thereby a simplified, approximated approach, in which the macroscopic polarization is defined as dipole moment per volume unit calculated with respect to a reference phase with $P_S = 0$ (e.g., the paraelectric phase). More details about the calculation of P_S are given elsewhere [2].

2.5 Electrical conductivity measurements

To determine electrical conductivity, the samples are mounted in a furnace using an alumina support. Temperature control is realized using a type B thermocouple located near the sample. Further, a Pt100 thermoresistor is used to compensate for the temperature fluctuations at the cold end of the thermocouple. The thermoelectric voltages are acquired by a digital voltmeter (Keithley-Instruments, USA). Measurements are conducted in air at atmospheric pressure up to 1623 K with a rate of 1 K/min. We perform short-term experiments in that sense that the dwell time at the maximum temperature is only one hour.

To determine the electrical impedance, the samples are connected by platinum foils and wires to an impedance/gain-phase analyzer (Solartron 1260, Ametek Scientific Instruments, Hampshire, UK). The impedance spectra are acquired in the frequency range from 1 Hz to 1 MHz with an excitation AC voltage of 50 mV.

The electrical conductivity of the samples is described by an equivalent circuit (EC) model consisting of a bulk resistance (R_B) in parallel to a constant phase element (CPE), inferred from the obtained single semicircle in the complex plane. The bulk resistance is derived by least squares fitting of the related model parameters. Figure 1 shows exemplarily data at 873 k and the fitted model function. The intersection of the fitted semicircle with the real impedance axis is interpreted as bulk resistance R_B and converted in the electrical conductivity $\sigma(T)$ according to $\sigma = l/(AR_B)$, where A and l are the electrode area and the distance between the electrodes. Note that the uncertainty of the conductivity measurements amounts to up to 8% [45]. Up to about 1000 K - 1230 K (depending on the specific sample) the exponent of the CPE is found to be in the range 0.9 - 1.0. Above this temperatures, the exponent of the CPE is smaller

than 0.9. Furthermore, the semicircles are less pronounced due to increasing inductive contributions. Nevertheless, the resistance can be determined as the intersection of fitted data and real impedance axis at the low-frequency side of the spectra.

The electrical conductivity σ can be described by a Arrhenius relation as follows:

$$\sigma = \sigma_0/T \exp(-E_A/(k_B T)) \quad (1)$$

Here, σ_0 , E_A , k_B and T represent a pre-exponential constant, the activation energy, the Boltzmann constant, and the absolute temperature, respectively. The factor $1/T$ reflects the correlation between mobility, relevant for electrical conductivity, and thermally activated diffusion according to the Nernst-Einstein relation.

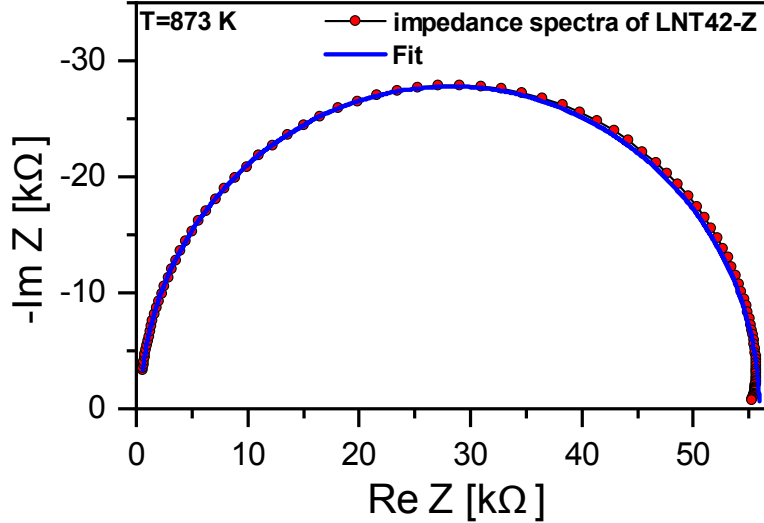


Figure 1: Example of an impedance spectra of sample LNT42-Z at 873 k in the frequency range from 10 Hz to 1 MHz. Beside data, the fit of the equivalent circuit model (see text) is shown.

3 Results

3.1 Specific heat capacity and Curie temperature

The DSC can be seen as a standard method to determine the specific heat capacity C_p . Here, the focus is on abrupt changes of C_p at the phase transitions temperature only. Fig. 2 depicts the $C_p(T)$ curves for LN, LNT42, LNT64, and LT, which show the respective specific heat capacities at different temperatures for each material. The highest peaks in the curves indicate the T_c of each material. Notably, LN exhibits the highest T_c value of 1415 K with LT42 and LT64 having T_c values of 1215 K and 1092 K, respectively. Lastly, LT has a T_c value of 873 K.

Fig. 3 shows the plot of T_c as a function of composition, along with literature data. A linear correlation between T_c and Ta content is evident. Upon comparison with the literature data, it is observed that LN in references [33], [3] and [1] exhibits T_c values of 1432 K, 1433 K, and 1423 K, respectively, while in this work, LN demonstrates a T_c of 1430 K. Similarly, for LT, The literature value for T_c are 923 K in references [33] and [3], 879 K in reference [1], and 873 K in this work. Notably, LNT42 and LNT64 exhibit commendable linear agreement with the established literature data.

The temperature dependence of the T_c data determined here can be approximated well by a linear function of the composition x according to

$$T_c = \alpha + \beta x. \quad (2)$$

with $\alpha = 1429$ K and $\beta = -546$ K.

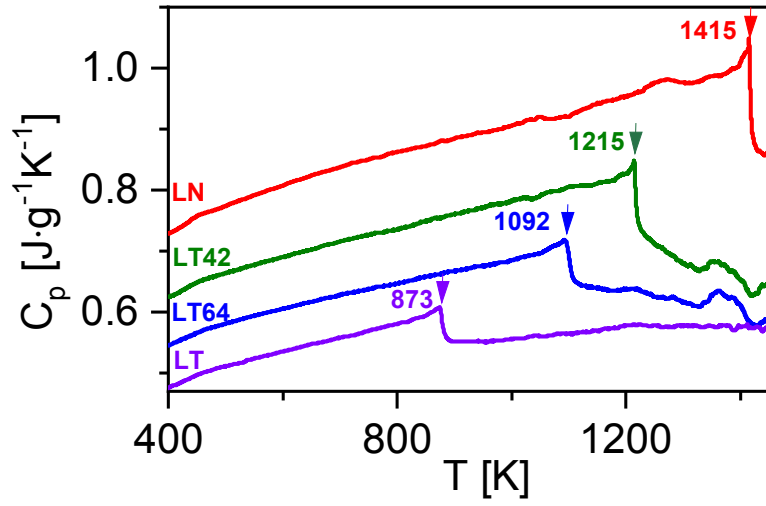


Figure 2: Experimental specific heat capacity of $\text{LiNb}_{1-x}\text{Ta}_x\text{O}_3$ measured in this study. The parameters indicate the Curie temperature of the respective sample.

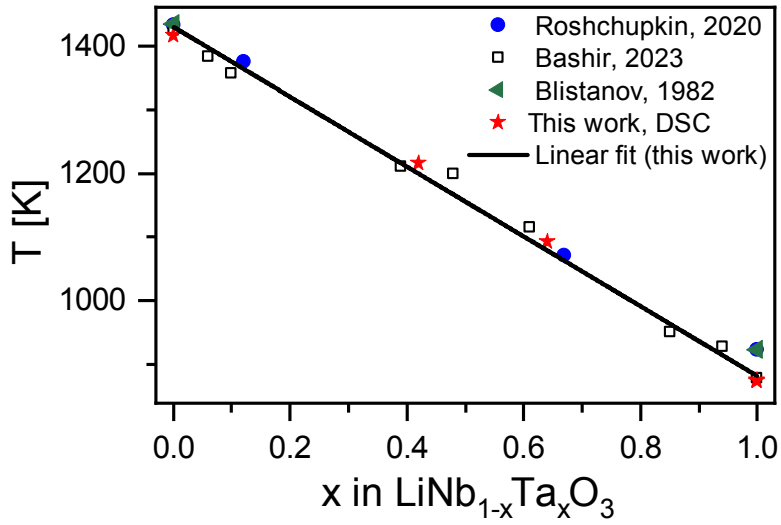


Figure 3: Curie temperature of $\text{LiNb}_{1-x}\text{Ta}_x\text{O}_3$ determined in this study, compared to literature data [33] (Roshchupkin, 2020), [1] (Bashir, 2023) and [3] (Blistanov, 1982).

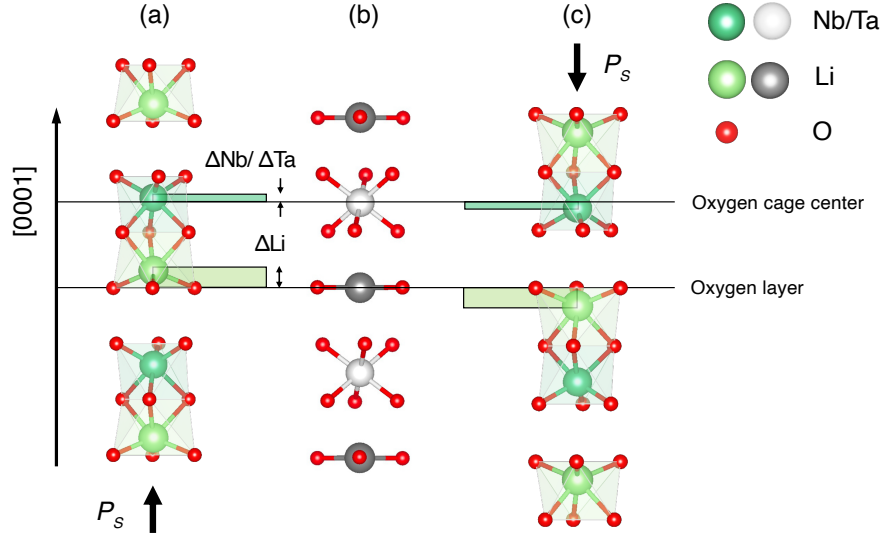


Figure 4: Atomic structure of the ferroelectric (a, c) and paraelectric (b) phase of LiNbO_3 and LiTaO_3 . The displacement of the Nb/Ta atoms from their positions in the paraelectric phase, i.e. from the center of the oxygen octahedra is denoted by ΔNb or ΔTa , whereas the displacement of the Li ions from the oxygen planes is labeled by ΔLi .

3.2 Molecular dynamics

AIMD runs have been performed at temperature intervals of 100 K from 300 K to 1100 K for LiTaO_3 and from 900 K to 1600 K for LiNbO_3 . From each MD trajectory, the displacements of Li and Nb/Ta from their equilibrium position in the paraelectric phase can be obtained. According to the $R\bar{3}C$ symmetry of the paraelectric phase, the equilibrium position of the Li ions is within a (0001) oxygen layer, while Ta/Nb ions are exactly at the center of the oxygen octahedra. This is shown schematically in Fig. 4.

The results from the AIMD are shown in Fig. 5. The displacement distribution of the Ta/Nb atoms as extrapolated from the AIMD is well approximated by a single gaussian curve, centered at 0 within the paraelectric phase and continuously shifted to higher values when the temperature decreases. The displacements of the Ta/Nb ions are limited to ca. 0.35 Å from their equilibrium position, demonstrating that both Nb and Ta remain within the oxygen octahedra and thus suggesting a limited mobility.

The displacement distribution of the Li ions reveals a striking different behavior, instead. At low temperatures, the Li ions are all above (or all below) an oxygen (0001) layer. All the displacements are again well fitted by a single gaussian curve. When the temperature increases, a fraction of the Li atoms possesses enough thermal energy to pass the oxygen layer. In the paraelectric phase, the Li atoms oscillate around the oxygen layer, thus continuously passing through the oxygen (0001) plane. The corresponding displacement distribution is bimodal and can be fitted by two gaussian curves.

On the one hand, this results in a dipole moment per unit cell that vanishes in average, explaining the absence of a spontaneous polarization at high temperatures. On the other hand, this shows the high mobility of the Li ions, confirming the common assumption that they are the main mobile ionic charge carriers, and the main carrier at all at moderate temperatures.

Interestingly, the AIMD shows that both for LiTaO_3 and LiNbO_3 substantial deviations from the equilibrium positions of the ferroelectric structure occur before T_C . In particular, Li ions display a non negligible mobility (a fraction of the ions passing the oxygen plane) already a temperature well below T_C , which might have an influence on the ionic conductivity.

In order to explore whether the Li mobility correlates with the electrical conductivity, the occupation of the Li octahedra is shown in Fig. 6 as a function of temperature. Details are discussed in Sec. 4.

For the interpretation of the AIMD results, a word of caution is in order. Atomistic calculations model ideal, stoichiometric materials. Real samples will feature a high density of point (intrinsic and extrinsic) and extended defects (dislocations, domain boundaries, etc.). In particular, if the congruent composition

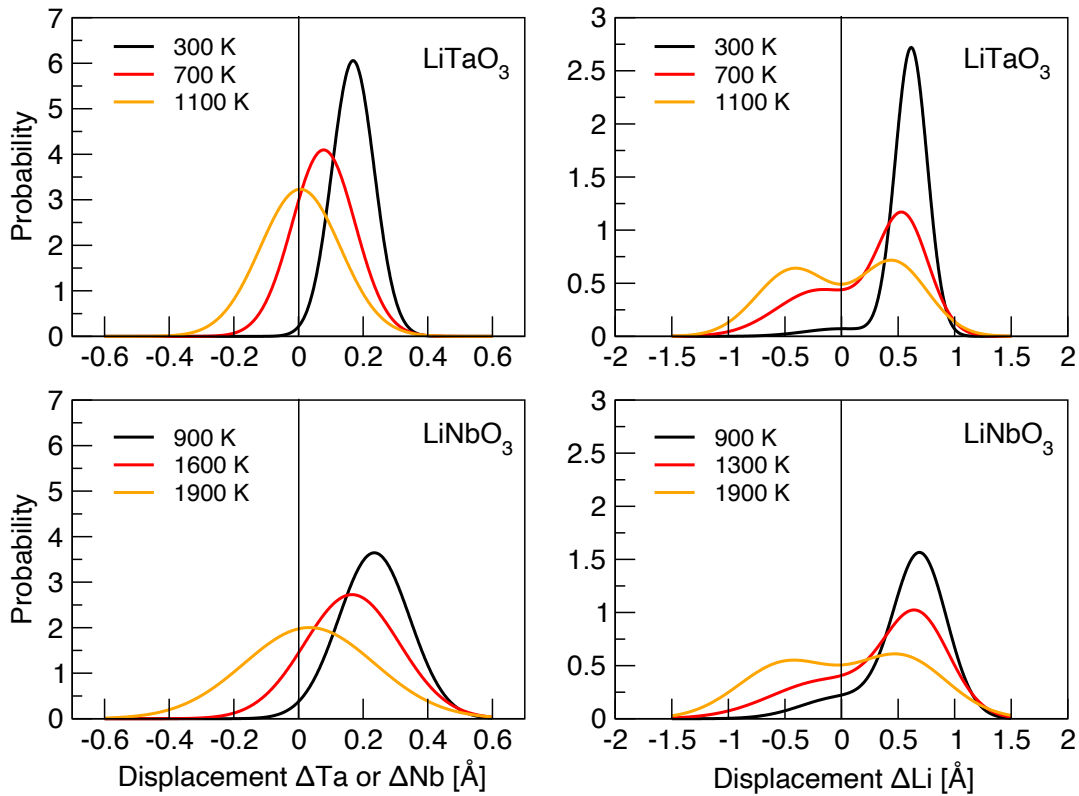


Figure 5: Left column: Probability distribution of the parameter ΔNb (representing the displacement of the Nb ions from the center of the oxygen octahedra) at different temperatures in LiTaO_3 and LiNbO_3 . The distribution is unimodal at every temperature, as expected for a displacive phase transition. Right column: Temperature dependent probability distribution of the parameter ΔLi (representing the displacement of the Li ions from the oxygen planes) in LiTaO_3 and LiNbO_3 . The unimodal distribution well below the Curie temperature suggests that all the Li ions are located above the oxygen planes. The symmetric, bimodal curve at above T_c indicates that the Li ions are randomly distributed above or under the oxygen planes, as expected for an order-disorder phase transition.

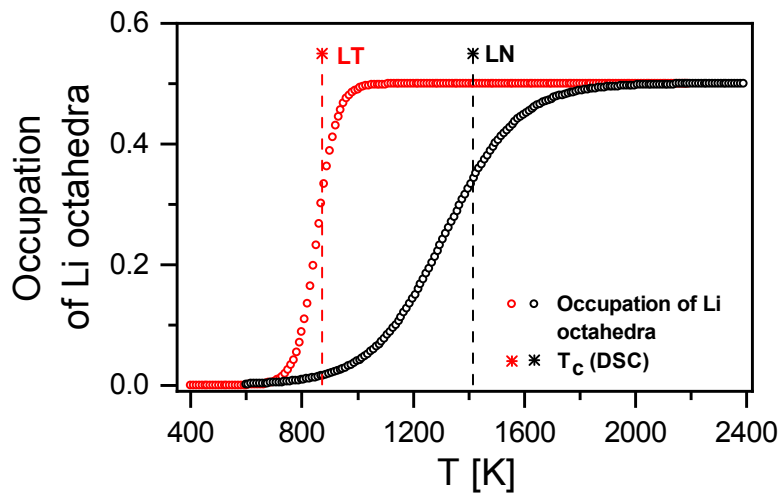


Figure 6: Calculated temperature dependent occupation of the regular Li octahedra (black triangles) and fit through a sigmoid function for LN and LT. Calculated data is rigidly shifted to match the measured T_c

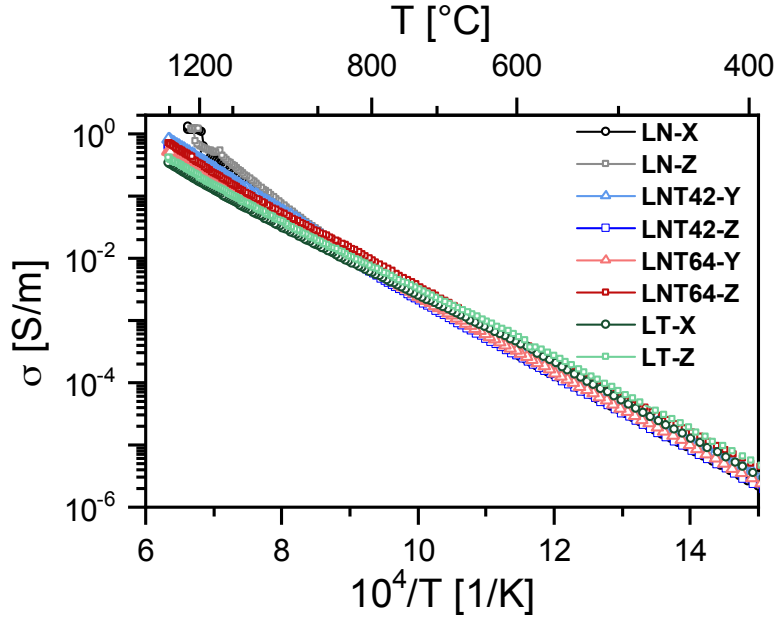


Figure 7: Arrhenius diagram showing electrical conductivities of LN, LT, and LNT samples along different crystallographic directions.

is considered, the presence of a high concentration of Li vacancies must be taken into account, which can heavily affect the conductivity.

3.3 Electrical conductivity

Figure 7 displays the electrical conductivity of LN and LT samples in both X and Z directions, as well as the Y and Z directions of LNT42 and LNT64 samples in air over a temperature range from 673 K to 1503 K in form of an Arrhenius representation. The data reveal a minor dependence of conductivity on composition up to about 873 K. Here, ionic conduction due to migration of lithium ions with an activation energy of about 1.3 eV dominates the electrical conductivity. The conclusion follows from the fact that lithium diffusion converted into electrical conductivity corresponds well to the electrical conductivity measured directly [7, 42, 17].

To visualize this observation in more detail, Fig. 8 shows the electrical conductivity as function of composition and crystallographic orientation for selected temperatures. Within the temperature range from 673 K to about 873 K, the composition has minor influence on electrical conductivity. Given that electrical conductivity measurements have an uncertainty up to 8%, we conclude that the composition does not significantly affect the conductivity in this temperature range. However, above this temperature, an additional contribution potentially occurs with decreasing LT content, as suspected from Figs. 7 and 8. However, based on the previous presentations, the increasing conductivity and, in particular, the related temperature ranges are difficult to evaluate.

A more comprehensive picture is achieved by calculation of the logarithmic slope $E_{\sigma T}$ from Eq. 1:

$$E_{\sigma T} = -k_B \frac{\partial \ln(\sigma T)}{\partial(1/T)}. \quad (3)$$

If a single conduction mechanism dominates in a sufficiently large temperature range, $E_{\sigma T}$ is constant and can be assigned to an activation energy E_A . The approach, in turn, reveals distinct temperature ranges for the electrical conductivity that are not fully recognizable in the Arrhenius representation.

Figure 9(a) shows the slopes $E_{\sigma T}$ of LNT for different compositions and crystal directions. A common observation is the independence of $E_{\sigma T}$ from the direction of the transport. Based on this, the simpli-

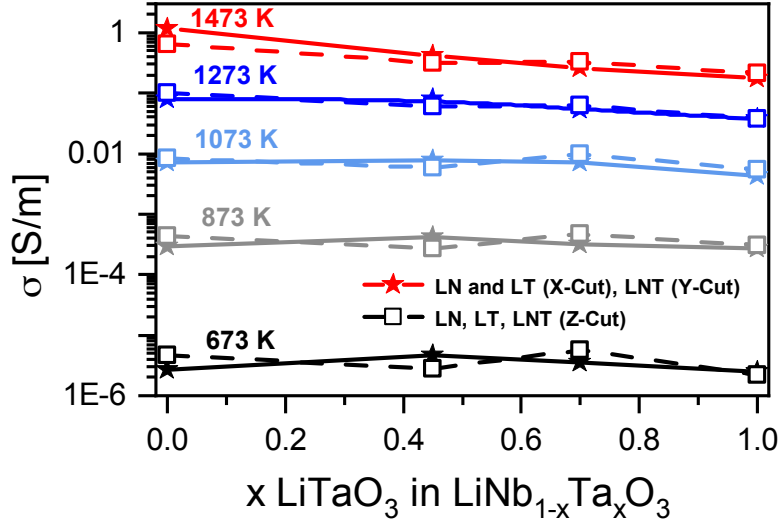


Figure 8: Electrical conductivities of LN, LT, and LNT samples along the crystallographic X, Y, and Z directions as a function of LT concentration.

fied Fig. 9(b) highlights characteristic features for the different compositions only. Additionally, Curie temperatures T_c obtained from the specific heat capacity are indicated by vertical lines for the respective composition. A key observation is the abrupt decrease of $E_{\sigma T}$ when passing the transition from the ferroelectric to the paraelectric phase. In addition, four characteristic temperature ranges can be recognized, on which the aforementioned decrease of $E_{\sigma T}$ is superimposed:

- (1) At relatively low temperatures from 673 K to about 873 K, $E_{\sigma T}$ is constant and represents the activation energy E_{AI} of the lithium migration mentioned above. Its values are determined by averaging $E_{\sigma T}$ and listed in Tab. 2 together with the associated specific temperature ranges. The values are represented as horizontal lines in Fig. 9(a).
- (2) With increasing temperature, a range with slightly increasing $E_{\sigma T}$ up to about 1073 K becomes visible. It is attributed to additional electronic conduction [45]. Note that the slope of $E_{\sigma T}$ depends on the composition, as discussed in the context of Figs. 7 and 8. For $x = 1$, a nearly constant slope follows, which enables to calculate the activation energies given in Tab.2. Note, that the latter belong to the paraelectric phase of LT.
- (3) An even stronger increase in $E_{\sigma T}$ is observed above 1073 K. It extends up to about 1273 K and 1573 K for LN and LT respectively. The nature of this contribution is not yet known and subject of ongoing investigations. In the short-term experiments carried out here, degradation obviously plays a minor role, as the data for heating and cooling differ very little.
- (4) Finally, a decrease of $E_{\sigma T}$ is observed with further increasing temperature. In case of LT, the decrease starts at about 1323 K and coincides with the drop at T_c . In case of the other compositions, the decrease starts at even higher temperatures, and is far off T_c .

A common phenomenological observation in the vicinity of the phase transitions is an increase in $E_{\sigma T}$ with temperature, which is superimposed by an abrupt drop of $E_{\sigma T}$ at the phase transition temperature. This situation enables the extraction of the magnitude of the drop in $E_{\sigma T}$. In the vicinity, but not at the phase transition temperature of a sample under consideration, the continuous change in $E_{\sigma T}$ can be approximated by a linear function. In addition, the abrupt change of $E_{\sigma T}$ at the phase transition must be taken into account. The following phenomenological description can be chosen:

$$E_{\sigma T} = E_0 + E_1 X + \frac{\Delta E}{1 + e^{w(X_0 - X)}} \quad (4)$$

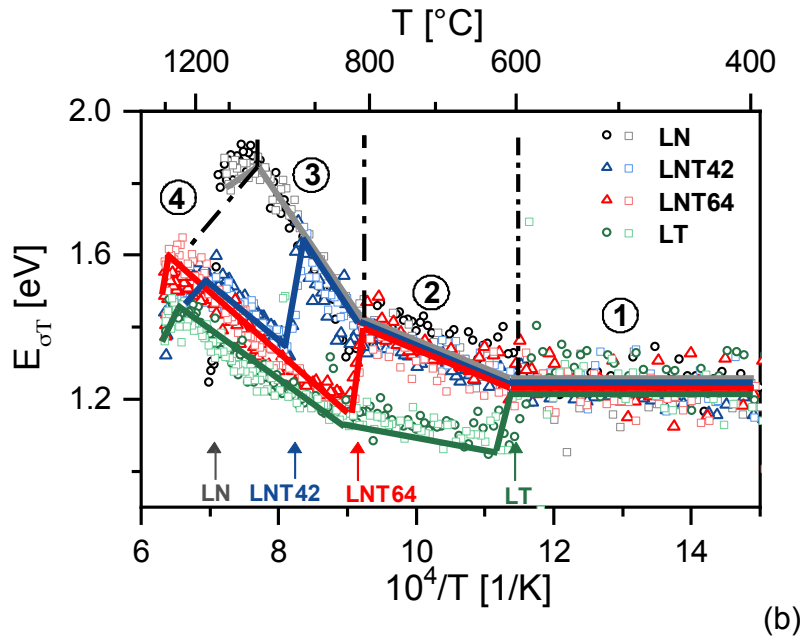
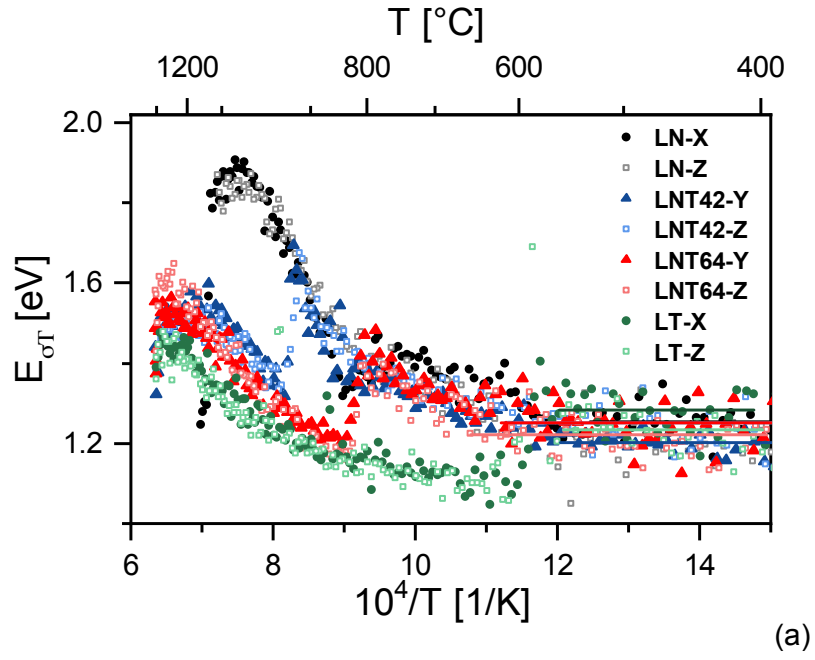


Figure 9: Logarithmic slopes of conductivity for representative LNT samples. Horizontal lines indicate approximately constant $E_{\sigma T}$ ranges (a). Scheme of the upper figure. The arrows indicate the Curie temperature for the respective composition while the dot-dash lines separate the temperature ranges discussed.

Table 2: Activation energies of lithium ion conductivity calculated by averaging $E_{\sigma T}$ in the given temperature range.

Sample name	Temperature range [K]	Activation energy E_{AI} [eV]
LT-X	673 - 843	1.23
	878 - 1073	1.13
LT-Z	673 - 843	1.28
	883 - 1073	1.12
LNT64-Y	673 - 853	1.24
LNT64-Z	673 - 883	1.22
LNT42-Y	673 - 853	1.20
LNT42-Z	420 - 923	1.25
LN-X	673 - 803	1.19
LN-Z	673 - 803	1.20

Table 3: The Curie temperature of LNT determined by DSC (numbers in bold), MD calculations (AIMD, SSCHA) and $E_{\sigma T}$ -values (averaged numbers for both directions in bold) along with a comparison of activation energies of conductivity during phase transformation. The sample name applies for the conductivity measurements only.

Composition	Method	DSC	AIMD	SSCHA	Conductivity			
					T_c [K]	ΔE [eV]	Sample	
1.0		873	841	808	870	862	0.181 \pm 0.002	LT-X
						877	0.181 \pm 0.011	LT-Z
0.64		1092	-	-	1092	1094	0.284 \pm 0.025	LNT64-Y
						1089	0.252 \pm 0.023	LNT64-Z
0.42		1215	-	-	1215	1218	0.333 \pm 0.027	LNT42-Y
						1212	0.314 \pm 0.028	LNT42-Z
0.0		1415	1524	1408	1410	1411	0.621 \pm 0.007	LN-X
						1408	0.800 \pm 0.005	LN-Z

Here, $X = 1/T$ and $X_0 = 1/T_0$ represent the reciprocal temperature in general and at the turning point of the sigmoid function used here to describe the width w and magnitude ΔE of the abrupt change in $E_{\sigma T}$. Furthermore, E_0 and E_1 are the coefficients of the linear function to approximate the continuous change.

Since the exact shape of the abrupt change in $E_{\sigma T}$ is unknown, the sigmoid function chosen here is a straight forward approximation that requires the least assumptions. The choice of such a function is justified if a closer look is taken at $E_{\sigma T}$ in the vicinity of the phase transition as done in Fig. 10. However, the relationship between reciprocal temperature and $E_{\sigma T}$ cannot be specified further due to scattering of the latter. Note, that the scatter results from the fact $E_{\sigma T}$ is a derivative.

The parameters of Eq. 4 are fitted to $E_{\sigma T}$. Beside ΔE , X_0 is relevant and discussed in relation to T_c . Here, w , E_0 and E_1 enable fitting, but are not used further. Figure 10 presents the fit of Eq. 4 to $E_{\sigma T}$ in the vicinity of the phase transition. The enlarged representation also shows no dependence on the crystal direction.

The numerical results of the fitting are summarized in Tab. 3 and compared with T_c from DSC and theory.

4 Discussion

The first and most remarkable result is the change in activation energy of the electrical conductivity upon the ferroelectric-paraelectric phase transition. The fact is discussed below in concert with the dependence of ΔE from composition.

The second key result is the agreement between the (reciprocal) turning points $1/X_0$ and the Curie temperatures determined from $E_{\sigma T}$ and DSC data, respectively, for a given composition. Consequently, $1/X_0$ represents the Curie temperature, in this case, derived from electrical conductivity. Accordingly, $1/X_0$ is also denoted as T_c in Tab. 3. The experimental data compared here are highlighted in bold in

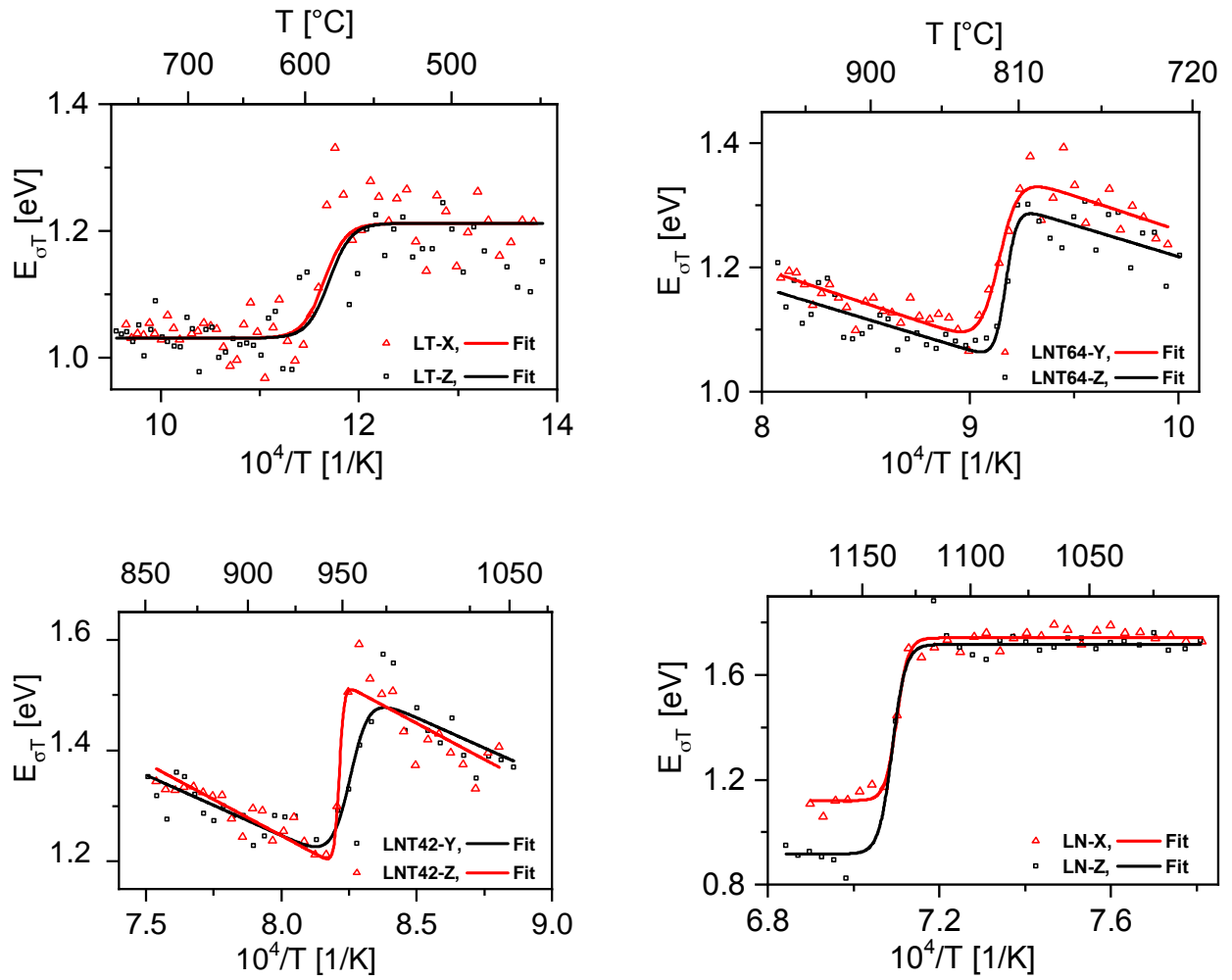


Figure 10: Representative slopes of logarithmic conductivity for samples of LNT (symbols) and fit (line) in the vicinity of the respective phase transition.

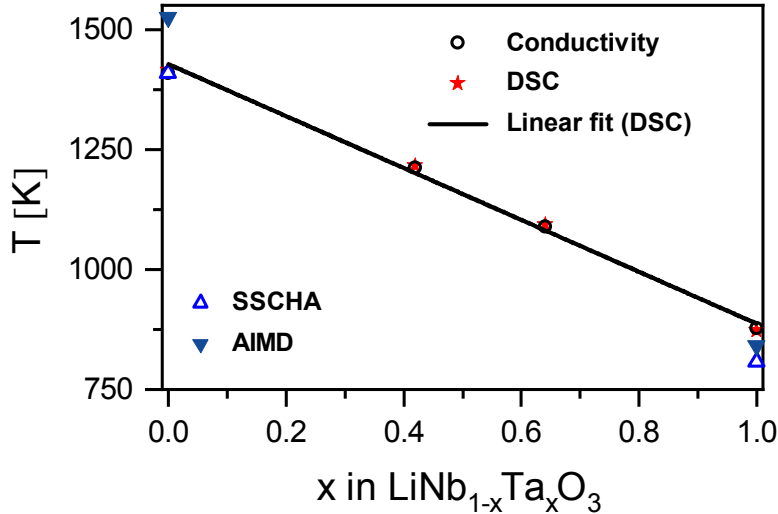


Figure 11: Curie temperatures of LNT determined experimentally (DSC, electrical conductivity) and calculated (SSCHA, AIMD). The linear fit for DSC data corresponds to that in Fig. 3.

Tab. 3. Furthermore, the situation is visualized in Fig. 11. The measured data are also in reasonable agreement with the theoretical estimate of T_c resulting from molecular dynamics or the SSCHA algorithm [2].

Thirdly, the abrupt drop ΔE in $E_{\sigma T}$ at the transition from the ferroelectric to the paraelectric phase increases with decreasing Ta content. The latter goes along with the increasing temperature of the phase transition.

The discussion of these results must be done based on the mechanisms of the charge transport. Up to about 600 °C, lithium migration dominates. Above that temperature, transport via free polarons contributes increasingly. This contribution depends on the composition, and is particularly significant in Nb rich LNT [45]. Consequently, the impact of the phase transition on both the ionic and electronic transport must be considered.

4.1 Effect of the phase transition on the ionic transport

The decrease of $E_{\sigma T}$ when exceeding the Curie temperature T_c is the most evident phenomenon in case of LT. Here, in the ferroelectric and the paraelectric phase below and above T_c , respectively, ranges with constant $E_{\sigma T}$ exist, which can be assigned to activation energies denoted by E_{AI} in Tab. 2. We attribute the decrease of the activation energy to the peculiar distribution of the Li ions on the octahedral sites, which are involved in the phase transition near T_c . The occupation of the octahedral sites depends on the temperature, as revealed by AIMD and shown in Figure 6.

Figure 12(a) shows the position of the Li ions and vacancies in the ferroelectric phase, as well as the preferred path (red arrow) for the Li migration with an activation energy of 1.29 eV [17]. In the paraelectric phase, the Li ions are expected with a probability of 0.5 in two adjacent positions, given respectively by the dark and light blue positions in Fig. 12(b) [36]. As a consequence, half of the moving Li vacancies no longer have to cross the repulsive oxygen plane (red line), resulting in a shorter transport path (black arrow). In the ferroelectric phase, the potential barrier has a maximum when the diffusion path leads the moving Li atoms between two Nb ions [17]. We suggest that the energy barrier for the Li diffusion in the paraelectric phase has a maximum at a similar position. However, the barrier height has a slightly lower average value due to the different distribution of the Li ions. The question of whether the specific difference of the activation energy of 0.181 eV below and above T_c can be explained in this way has to be clarified by further atomistic calculations.

As long as the contribution of electrons to the electrical conductivity is low, the decrease in activation

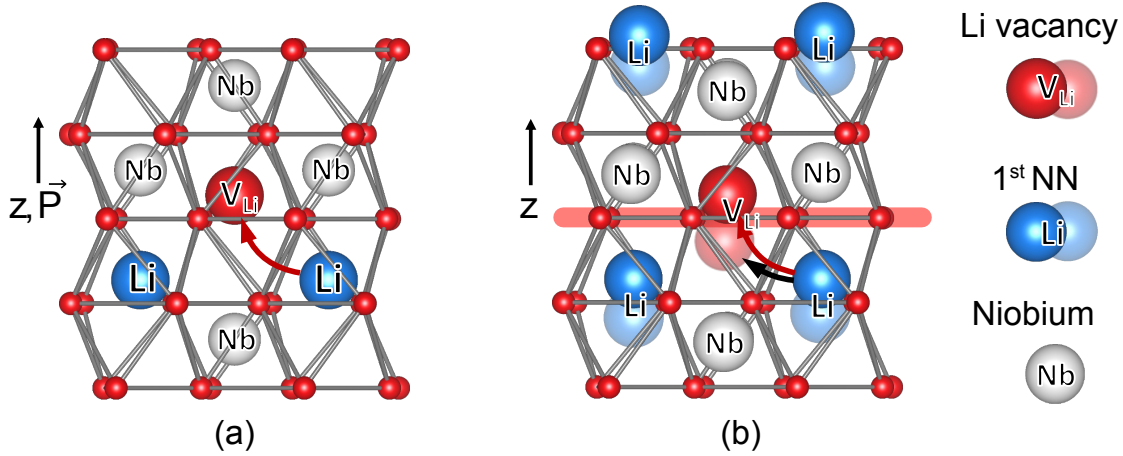


Figure 12: Position of the Li ions and vacancies in the ferroelectric phase [Ref12] (a) and paraelectric phase with Li ions expected with a probability of 0.5 in two adjacent positions (dark and light blue) (b).

energy is seen as an effect of the Li transport. The condition is fulfilled for LT around 870 K.

4.2 Effect of the phase transition on the electronic transport

Electronic transport in LN is usually interpreted in terms of polaron hopping. A polaron is formed in materials with high lattice polarizability, when the lattice deformation induced by a charge carrier is strong enough to localize the carrier substantially at a single lattice site (small polaron). Charge carriers (electrons or holes, in LN and LT mostly electrons) localized at a regular lattice site are referred to as free small polarons, whereas they are referred to as bound polarons if they are localized at a lattice defect. Due to the lattice distortion, tunneling to equivalent lattice sites is strongly quenched, and only thermally activated hopping allows transport to neighboring sites. Transport can occur in form of hopping, when an activation energy between the initial and final state is overcome. In the case of free polarons, thermally induced phonon excitations might render the electronic energies of the two sites equal, so that a transition between both states by tunneling is greatly facilitated.

Differently from free polarons, the coupling to a single point defect removes the Bloch character from bound polarons. The binding to the defect by coulomb interaction causes a more pronounced distortion-related localization and stabilization. Moreover, the presence of the defect causes an inequivalence between the initial and the available final states of a hopping process. Thus, the mixture of initial and final states is asymmetric, strongly reducing the intensity of a charge transfer transition.

The polaronic contribution to electronic transport is therefore expected to stem mainly from free polarons [38], which might become rather mobile at higher temperatures, at which thermal fluctuations of the lattice generate configurations in which the electron energies at the initial and the final sites are equal.

Another aspect that could contribute to the decrease of the activation energy during the transition from the para- to the ferroelectric phase is the narrowing of the band gap accompanying the transition. Many-body perturbation theory indicates a decrease of the band gap energy by 0.5 eV for LN, for example [40]. This decrease supports the excitation of electrons, which in turn contribute to polaron transport.

4.3 Comparison of experiments and atomistic calculations

Temperature dependent DSC data and the slope of the electrical conductivity $E_{\sigma T}$ of LN and LT are compared in Fig. 13. The Curie temperatures determined experimentally by both methods agree very well, see also Tab. 3. This statements holds true for LNT crystals, too. Consequently, the evaluation of the electrical conductivity is an elegant approach to determine the Curie temperature as the turning point of the fitted sigmoid function, respective T_c , is clearly visible in the measurements carried out here.

Furthermore, Fig. 13 encloses the temperature dependent polarization of LN and LT as calculated from the AIMD trajectories [2]. The AIMD determined onset of the spontaneous polarization at 841 K and

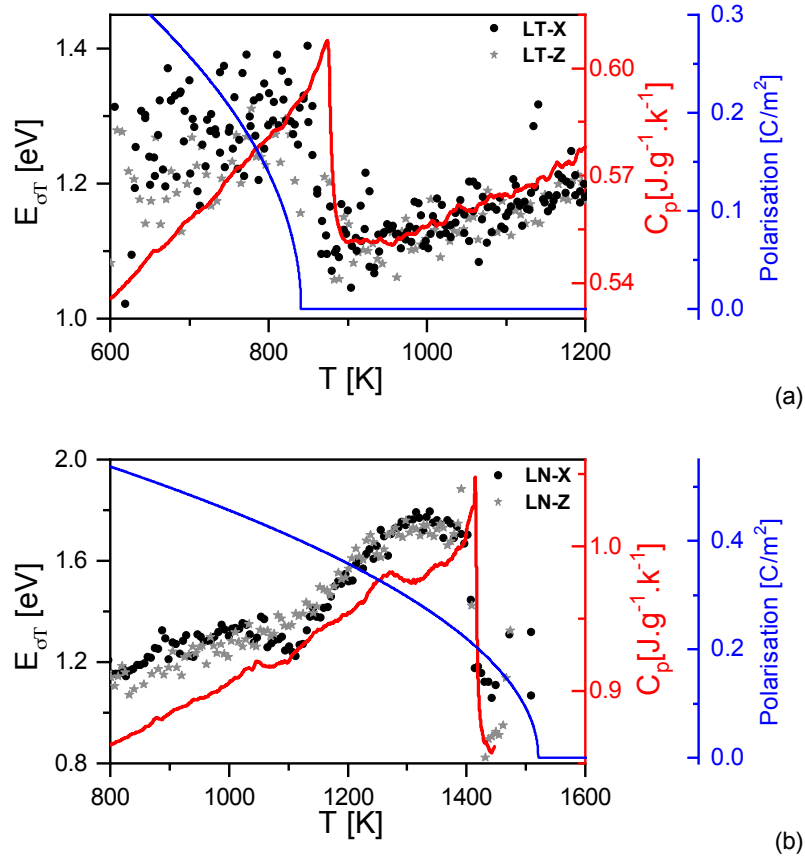


Figure 13: Calculated spontaneous polarisation as a function of temperature (blue line), measured electrical conductivity (symbol) and measured thermal capacity at constant pressure $C_p(T)$ (red line) of LiTaO_3 (a) and LiNbO_3 (b).

1524 K for LT and LN, respectively, corresponds roughly to the range at which the activation energy of the electrical conductivity changes from the value of the paraelectric to the value of the ferroelectric phase. In the case of LT, the AIMD calculations result in T_c that matches the experimental values reasonably well. Here, the activation energy of the electrical conductivity decreases between 830 K and 890 K. The related change of C_p is observed between 873 K and 890 K. In the case of LN, however, the AIMD calculations overestimate T_c , resulting in a small deviation from the experimental values. Here, the changes of $E_{\sigma T}$ and C_p are observed between 1390 K and 1443 K and between 1415 K and 1443 K, respectively. Based on the calculated and measured data, it can be concluded that the phase transition is a continuous process that affects the properties of the materials below the critical temperature T_c .

5 Conclusions

An investigation of the ferroelectric to paraelectric phase transition of $\text{LiNb}_{1-x}\text{Ta}_x\text{O}_3$ is presented, which revealed a linear dependence of the phase transition temperature near T_c on the composition x . Beside differential scanning calorimetry data, the slope of the electrical conductivity is evaluated. The latter enables to extract T_c . Consequently, the measurement of the electrical conductivity is an elegant approach to determine T_c . Further, the conductivity slope reveals a significant change in activation energy during the transition. The observation is, on the one hand, attributed to the peculiar distribution of the Li ions on the octahedral sites which affects the Li ion transport. On the other hand, with rising temperatures and, in particular, for low Ta content x , the transport of polarons contributes increasingly to the total conductivity. Here, lattice distortion is expected to affect the hopping of polarons. The latter might become rather mobile at higher temperatures and, consequently, thermal fluctuations of the lattice generate configurations in which the electron energies at the initial and the final sites are equal, thus facilitating

polaron hopping. Furthermore, molecular dynamics calculations within the framework of the density functional theory show that substantial cation displacements occur below the transition temperature for both LiNbO_3 and LiTaO_3 , and presumably $\text{LiNb}_{1-x}\text{Ta}_x\text{O}_3$. These displacements might, therefore, affect the properties of the materials already below T_c .

Acknowledgements

The Deutsche Forschungsgemeinschaft (DFG, German Research Foundation) is gratefully acknowledged for financial support within the research unit FOR5044 (GA 2403/7-1, FR 1301/40-1, FR 1301/42-1, SA 1948/2-1). In addition, the authors thank the Research Center Energy Storage Technologies (Forschungszentrum Energiespeichertechnologien) for support. Calculations for this research were conducted on the Lichtenberg high-performance computer of the TU Darmstadt and at the Höchstleistungsrechenzentrum Stuttgart (HLRS). The authors furthermore acknowledge the computational resources provided by the HPC Core Facility and the HRZ of the Justus-Liebig-Universität Gießen.

References

- [1] U. Bashir, K. Böttcher, D. Klimm, S. Ganshow, F. B. S. Sanna, M. Rüsing, L. M. Eng, and M. Bickermann. *Ferroelectrics*, 613(1):250–262, 2023.
- [2] F. Bernhardt, C. Fink, L. M. Verhoff, N. A. Schäfer, A. Kapp, W. A. Nachwati, U. Bashir, F. E. Azzouzi, U. Yakhnevych, Y. Suhak, K.-D. Becker, D. Klimm, S. Ganschow, H. Schmidt, H. Fritze, and S. Sanna. *Phys. Rev. M*, 2024.
- [3] A. A. Blistanov, V. S. Bondarenko, N. V. Perelomova, F. N. Strizhevskaya, V. V. Chkalova, and M. P. Shaskolskaya. *Acoustic crystals*. Nauka, Moscow, 1982.
- [4] P. E. Blöchl. *Phys. Rev. B*, 50:17953–17979, 1994.
- [5] P. F. Bordui, R. G. Norwood, C. D. Bird, and G. D. Calvert. *Journal of Crystal Growth*, 113:61–68, 1991.
- [6] C. Campbell. *Surface Acoustic Wave Devices and Their Signal Processing Applications*. San Diego: Academic Press, 1989.
- [7] R. H. Chen, L. Chen, and C. Chia. *J. Phys. Condens. Matter*, 19:086225, 2007.
- [8] Y.-L. Chen, J.-J. Xu, X.-J. Chen, Y.-F. Kong, and G.-Y. Zhang. *Optics Communications*, 188(5):359–364, 2001.
- [9] C. Dues, M. J. Müller, S. Chatterjee, C. Attacalite, and S. Sanna. Nonlinear optical response of ferroelectric oxides: First-principles calculations within the time and frequency domains. *Phys. Rev. Mater.*, 6:065202, Jun 2022.
- [10] G. J. Friel, R. S. Conroy, A. J. Kemp, B. D. Sinclair, and J. M. Ley. *Appl. Phys. B—Lasers and Optics*, 67:267–270, 1998.
- [11] B. L. Holian, A. F. Voter, and R. Ravelo. *Phys. Rev. E*, 52:2338–2347, 1995.
- [12] J. Imbrock, S. Wevering, K. Buse, and E. Krätzig. *Journal of the Optical Society of America B*, 16:1392–1397, 1999.
- [13] E. R. J Hornsteiner, E Born. *Physica Status Solidi A*, 163:R3–R5, 1997.
- [14] D. Joubert. *Physical Review B - Condensed Matter and Materials Physics*, 59(3):1758–1775, 1999.
- [15] S. Kim and V. Gopalan. *J. Appl. Phys*, 90:2949 – 2963, 2001.
- [16] D. Kip. *Appl. Phys. B—Lasers and Optics*, 67:131–150, 1998.

- [17] C. Kofahl, L. Doörrer, B. Muscutt, S. Sanna, S. Hurskyy, U. Yakhnevych, Y. Suhak, H. Fritze, S. Ganschow, and H. Schmidt. *Physical Review Materials*, 7(033403):26–29, 2023.
- [18] J. Koskela, J. V. Knuuttila, P. T. Tikka, C. S. Hartmann, V. P. Plessky, and M. M. Salomaa. *Appl. Phys. Lett*, 75:2683–2685, 1999.
- [19] S. Kostritskii, M. Aillerie, P. Bourson, and D. Kip. *Appl Phys B*, 95:125–130, 2009.
- [20] S. M. Kostritskii and D. Kip. *Phys. Status Solidi A.*, 169:171–180, 1998.
- [21] A. Krampf, M. Imlau, Y. Suhak, H. Fritze, and S. Sanna. *New J. Phys.*, 23:033016, 2021.
- [22] G. Kresse and J. Furthmüller. *Computational Materials Science*, 6(1):15–50, 1996.
- [23] G. Kresse and J. Furthmüller. *Physical Review B - Condensed Matter and Materials Physics*, 54:111690–011186, 1996.
- [24] G. Kresse and J. Hafner. *Physical Review B*, 47:558–561, 1993.
- [25] G. Malovichko, V. Grachev, and O. Schirmer. *Appl. Phys. B*, 68:785–793, 1999.
- [26] W. P. Mason and R. Thurston. *Physical Acoustics*, volume 6. Academic press, New York, 1970.
- [27] R. C. Miller and W. A. Nordland. *American Physical Society*, B2:4896, 1970.
- [28] M. Nakamura, S. Takekawa, S. Kumaragurubaran, and K. Kitamura. *Japanese Journal of Applied Physics*, 47(5R):3476, 2008.
- [29] S. Nose. *The Journal of Chemical Physics*, 81:511–519, 1984.
- [30] J. P. Perdew, A. Ruzsinszky, G. I. Csonka, O. A. Vydrov, G. E. Scuseria, L. A. Constantin, X. Zhou, and K. Burke. *Physical Review Letters*, 100:1–4, 2008.
- [31] S. R. Phillpot and V. Gopalan. *Applied Physics Letters*, 84:1916–1918, 2004.
- [32] A. Räuber. *Chemistry and physics of lithium niobate*, volume 1 of *Current Topics in Materials Science*. Elsevier Science Publishing, Amsterdam, 1978.
- [33] D. Roshchupkin, E. Emelin, O. Plotitsyna, F. Rashid, D. Irzhak, V. K. Tatiana, O. N. Targonskaya, S. Sakharov, A. Mololkin, B. Redkin, H. Fritze, Y. Suhak, D. Kovalev, S. Vadilonga, L. Ortega, and W. Leitenberger. *Acta Cryst*, B76:1071–1076, 2020.
- [34] D. Royer and E. Dieulesaint. *Ondes Elastiques Dans Les Solides*. Masson, Paris, 1974.
- [35] S. Sanna and W. G. Schmidt. *IEEE Transactions on Ultrasonics, Ferroelectrics, and Frequency Control*, 59:1925–1928, 2012.
- [36] S. Sanna and W. G. Schmidt. *IEEE Transactions on Ultrasonics, Ferroelectrics, and Frequency Control*, 59:1925–1928, 2012.
- [37] S. Sanna and W. G. Schmidt. *Journal of Physics: Condensed Matter*, 29(41):413001, 2017.
- [38] O. Schirmer, M. Imlau, C. Merschjahn, and B. Schike. *J. Phys.: Condens. Matter*, 21:123201, 2009.
- [39] G. L. Tangonan, M. K. Barnoski, J. F. Lotspeich, and A. Lee. *Appl. Phys. Lett.*, 30:238–239, 1977.
- [40] C. Thierfelder, S. Sanna, A. Schindlmayr, and W. G. Schmidt. *Phys. Status Solidi C*, 7(2):362–365, 2010.
- [41] T. Volk and M. Wöhlecke. *Lithium Niobate: Defects, Photorefraction and Ferroelectric Switching*. Springer, Berlin, 2008.

- [42] A. Weidenfelder, J. Shi, P. Fielitz, G. Borchardt, K. D. Becker, and H. Fritze. *Solid State Ion*, 225:26–29, 2012.
- [43] V. Wong and M. C. Gupta. *J. Appl. Phys*, 84:6513–6518, 1998.
- [44] D. Xue, K. Betzler, and H. Hesse. *Solid State Communications*, 115:581–585, 2000.
- [45] U. Yakhnevych, F. E. Azzouzi, F. Bernhardt, C. Kofahland, Y. Suhak, S. Sanna, K. D. Becker, H. Schmid, S. Ganschow, and H. Fritze. *Solid State Ionics*, *submitted*, 2023.
- [46] H. Zu, H. Wu, and Q.-M. Wang. *IEEE Transactions on Ultrasonics, Ferroelectrics, and Frequency Control*, 63:486–505, 2016.